In-Flight Validation of Mid- and Thermal Infrared Data From the Multispectral Thermal Imager (MTI) Using an Automated High-Altitude Validation Site at Lake Tahoe CA/NV, USA

Simon J. Hook, William B. Clodius, Lee Balick, Ronald E. Alley, Ali Abtahi, Robert C. Richards, and S. Geoffrey Schladow

***Abstract*—The Multispectral Thermal Imager (MTI) is a 15-band satellite-based imaging system. Two of the bands (J, K) are located in the mid-infrared (3–5 μm) wavelength region: J, 3.5–4.1 μm and K, 4.9–5.1 μm, and three of the bands (L, M, N) are located in the thermal infrared (8–12 μm) wavelength region: L, 8.0–8.4 μm; M, 8.4–8.8 μm; and N, 10.2–10.7 μm. The absolute radiometric accuracy of the MTI data acquired in bands J-N was assessed over a period of approximately three years using data from the Lake Tahoe, CA/NV, automated validation site. Assessment involved using a radiative transfer model to propagate surface skin temperature measurements made at the time of the MTI overpass to predict the vicarious at-sensor radiance. The vicarious at-sensor radiance was convolved with the MTI system response functions to obtain the vicarious at-sensor MTI radiance in bands J–N. The vicarious radiances were then compared with the instrument measured radiances. In order to avoid any reflected solar contribution in the mid-infrared bands, only nighttime scenes were used in the analysis of bands J and K. Twelve cloud-free scenes were used in the analysis of the data from the mid-infrared bands (J, K), and 23 cloud-free scenes were used in the analysis of the thermal infrared bands (L, M, N). The scenes had skin temperatures ranging between 4.4 and 18.6 °C. The skin temperature was found to be, on average, 0.18 ± 0.36 °C cooler than the bulk temperature during the day and 0.65 ± 0.31 °C cooler than the bulk temperature at night. The smaller skin effect during the day was attributed to solar heating. The mean and standard deviation of the percent differences between the vicarious (predicted) at-sensor radiance convolved to the MTI bandpasses and the MTI measured radiances were -1.38 ± 2.32, -2.46 ± 1.96, -0.04 ± 0.78, -1.97 ± 0.62, -1.59 ± 0.55 for bands J–N, respectively. The results indicate that, with the exception of band L, the instrument measured radiances are warmer than expected.**

***Index Terms*—Calibration, radiance, temperature, thermal infrared, validation.**

Manuscript received June 11, 2004; revised January 6, 2005. This work was performed in part at the Jet Propulsion Laboratory, California Institute of Technology, under contract with the Los Alamos National Laboratory. Reference herein to any specific commercial product, process, or service by trade names, trademark, manufacture, or otherwise does not imply endorsement by the United States or the Jet Propulsion Laboratory, California Institute of Technology.

S. J. Hook, R. E. Alley, and A. Abtahi are with the Jet Propulsion Laboratory, California Institute of Technology, Pasadena, CA 91109 USA.

W. B. Clodius and L. Balick are with the Los Alamos National Laboratory, Los Alamos, NM 87545 USA.

R. C. Richards is with the Tahoe Research Group, Department of Environmental Science and Policy, University of California, Davis, CA 95616 USA.

S. G. Schladow is with the Department of Civil and Environmental Engineering University of California, Davis, CA 95616 U.S.A.

Digital Object Identifier 10.1109/TGRS.2005.853191

I. Introduction

THE Multispectral Thermal Imager (MTI) is a satellite-based pushbroom system with 15 spectral bands [10]. Each band is identified by a letter, two of the bands are located in the mid-infrared wavelength region: J, 3.5–4.1 μm and K, 4.9–5.1 μm, and three of the bands are located in the thermal infrared wavelength region: L, 8.0–8.4 μm; M, 8.4–8.8 μm; and N, 10.2–10.7 μm. The detectors for the 15 spectral bands are mounted on a single cryogenically cooled focal plane and use interference filters. The bands are implemented on three separate identical groups of detectors, termed sensor chip assemblies (SCAs). Each SCA can be thought of as a separate pushbroom sensor that contains a full set of the MTI bands, and covers a little over one third of the cross track field of view of the system. The system has a 36-cm aperture telescope with a nominal Ground Sample Distance (GSD) in the mid- and thermal infrared bands of 20 m. The mid- and thermal infrared bands use indium antimonide (InSb) and mercury cadmium telluride (HgCdTe) detectors respectively. The system also includes an extensive onboard calibration system that was lost shortly after launch.

The MTI satellite is in a sun-synchronous orbit and can take two images of a site in a single overpass: one near nadir and one near 60 ° off-nadir. MTI was launched on March 12, 2000, and performance was nominal until November 1, 2000, when the MTI temperature and calibration (TCAL) control system ceased functioning. On November 11, 2001 and again on May 24, 2003, MTI accidentally imaged the Sun for a few seconds. In both Sun looks, the resulting damage was largely confined to SCA 2. Vicarious calibration techniques are being used to correct for much of the resulting damage and loss of the calibration system.

MTI data are useful for a wide variety of studies including those requiring high spatial resolution water surface temperature measurements. Knowledge of the temperature distribution in water bodies is very valuable for understanding a variety of processes such as wind-induced upwelling events [13]–[15] and surface water transport patterns [21], [22]. The MTI project has developed a variety of algorithms for recovering the surface temperature of water, and the success of these algorithms depends, in part, on the on-orbit calibration of the instrument. This work utilizes an existing thermal infrared validation site at Lake Tahoe CA/NV to validate the radiometric accuracy of the data acquired by the MTI mid- and thermal infrared bands.

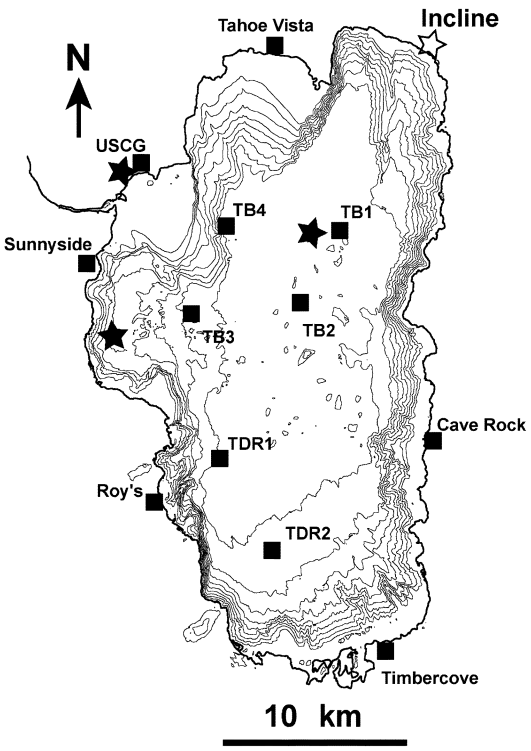

Fig. 1. Bathymetric map of Lake Tahoe with a contour interval of 50 m. The four NASA buoys are labeled TB1, TB2, TB3, and TB4. The two UCD rafts are labeled TDR1 and TDR2. Water properties are regularly measured by boat at the Midlake station (star near TB1) and the Index station (star south of Sunnyside) by UCD. Also shown around the edge of the lake are the USCG station (closed star), Incline (open star), and other locations (closed boxes) where meteorological measurements are made.

II. Site Location and Characteristics

Lake Tahoe is a large lake situated in a granite graben near the crest of the Sierra Nevada Mountains on the CA/NV border, at 39°N, 120°W. The lake level is approximately 1895 m above mean sea level. The lake is roughly oval in shape with a north–south major axis (33 km long, 18 km wide), and has a surface area of 500 km^2 (Fig. 1). The land portion of the watershed has an area of 800 km^2. Lake Tahoe is considered a deep lake, with an average depth of 330 m, maximum depth of 501 m, and a total volume of 156 km^3 (it is the 11th deepest lake in the world). The surface layer of Lake Tahoe deepens during the fall and winter. Complete vertical mixing only occurs every few years. Due to its large thermal mass Lake Tahoe does not freeze in winter. There are approximately 63 streams/rivers flowing into Lake Tahoe and only one river flowing out.

III. Site Infrastructure and Field Measurements

The Lake Tahoe CA/NV automated validation site was established in 1999 to help validate the thermal infrared data and products from the Advanced Spaceborne Thermal Emission and Reflectance Radiometer (ASTER) and Moderate Resolution Imaging Spectroradiometer (MODIS) instruments on the Terra spacecraft launched in 1999 [18] and [23]. The site is also being used to validate data from other sensors including the Along Track Scanning Radiometer-2 [8], Landsat ETM+ [1], and Landsat-5 [9]. Work at the site is performed by the Jet Propulsion Laboratory (JPL) and the University of California, Davis (UCD). A detailed description of the site is given in [8] and summarized here for completeness. Measurements at the site are made from four permanently moored buoys on the lake referred to as TB1, TB2, TB3, and TB4 and the U.S. Coast Guard (USGC) station located on the northwest shore of the lake (Fig. 1). Each buoy has a custom-built radiometer that measures the skin temperature and several temperature sensors that measure the bulk water temperature. The radiometers were built by JPL and two radiometer models have been deployed at the site. The earlier model had an accuracy of ± 0.2 °C and the later model has an accuracy of ± 0.1 °C. The radiometers are calibrated in the laboratory using a National Institute of Standards and Technology (NIST) traceable stirred water bath blackbody (Table I). The accuracy of the JPL radiometers was independently verified in both the laboratory and in a field comparison [2], [17]. The results indicate the JPL radiometers agree with other well calibrated radiometers to better than 0.1 °C [2]. The bulk temperature measurements are made by several different temperature sensors mounted ~ 2 cm beneath the surface on a floating support tethered behind each buoy. Details of the types of temperature sensor and their accuracies are summarized in Table II. The accuracies provided in Table II are from the manufacturer's specification prior to recalibration at the JPL facility. The temperature sensors are recalibrated at JPL using a temperature controlled water bath with a NIST traceable thermometer (Table I). During the monitoring period, meteorological stations were added to each buoy. The meteorological measurements include wind speed, wind direction, relative humidity, air temperature atmospheric pressure and net radiation. A full set of measurements (meteorology, bulk and skin temperatures) are made every 2 min and stored on data loggers which are read out either daily via telephone modem or every few months during site visits.

Both NASA/JPL and UCD maintain additional equipment at the USGC Station. This includes a full meteorological station (wind speed, wind direction, relative humidity, air temperature,

TABLE I
Specifications of the NIST Traceable Stirred Water Bath Blackbody Used to Calibrate the JPL Radiometers and the Temperature-Controlled Water Bath With NIST Traceable Thermometer Used to Calibrate the Sensors Used to Measure the Bulk Water Temperature. An Additional Secondary Temperature Probe Is Used Periodically to Cross-Check the Calibration of the Primary Temperature Probe

Component	Accuracy	Stability	Precision
NIST designed cone in a 44 liter temperature controlled bath (Model 7008-IR)		at 25° C: +/- 0.0007° C	
Thermistor standard probe (Model 5643-R)	0.0015 ° C over 0-60 ° C	0.005 ° C / yr	
Readout system (Chub E4)	0.0025 ° C at 25 ° C	.	0.0001 ° C

TABLE II
Manufacturer's Specifications for the Bulk Water Temperature Sensors Used at the Lake Tahoe CA/NV Site. Note all Sensors Are Recalibrated at the JPL NIST Traceable Calibration Facility (See Table I for Specifications of JPL Calibration Equipment)

Company	Sensor	Accuracy (Operating range Tahoe 4-25 C)	Resolution	Storage
Onset	Optic Stowaway	± 0.25° C	8-bit	32 kb
Onset	Hobo Water Pro	± 0.20° C	12-bit	32 kb
Onset	HOBO Pro Temp/External Temp	± 0.20° C	12-bit	64 kb
Apprise	MBLTA	± 0.10° C	12-bit	N/A

TABLE III
LATITUDE AND LONGITUDE POSITION OF THE LAKE TAHOE CA/NV NASA BUOYS. NOTE THE TWO SOUTHERN BUOYS WERE MOVED SLIGHTLY SOUTH IN LATE OCTOBER AND EARLY NOVEMBER 2002. LOCATIONS ARE GIVEN FOR THE BUOYS BEFORE AND AFTER THEY WERE MOVED

Buoy	05-07-1999 to present	06-16-1999 to present	05-07-1999 to 11-01-2002	11-01-2002 to present	06-16-1999 to 10-31-2002	10-31-2002 to present
TB1	39° 09.180 N 120° 00.020 W					
TB2			39° 08.292 N 120° 00.018 W	39° 06.562 N 120° 00.645 W		
TB3					39° 08.300 N 120° 04.920 W	39° 06.612 N 120° 04.521 W
TB4		39° 09.300 N 120° 04.330 W				

and atmospheric pressure), full radiation station (long and shortwave radiation up and down), a shadow band radiometer, and an all-sky camera. The shadow band radiometer provides information on total water vapor and aerosol optical depth. UCD also maintains two additional floats (rafts) in the southern part of Lake Tahoe (Fig. 1) which measure meteorological variables and bulk temperature.

The latitudes and longitudes of the four NASA buoys are given in Table III. TB2 and TB3 were moved slightly farther south during the monitoring period, and Table III gives the positions before and after the move.

Additional measurements including primary productivity, nutrient concentration (various forms of nitrogen and phosphorus), chlorophyll concentration, light penetration, temperature distribution and secchi disk transparency are made from the UCD Research Vessel John leConte at approximately ten-day intervals at the Midlake and Index stations (Fig. 1).

IV. MTI IMAGE DATA PROCESSING

A. Lake Tahoe Image Acquisition Process

The MTI is a snapshot store and forward system and has to be explicitly commanded to acquire an image of a site. The commands are uploaded up to two weeks before the image is acquired and include the time at which the image is to be acquired, the latitude and longitude of the site to be imaged, the along track length of the image, and the bands to be acquired for the image. The time of the acquisition is the predicted time of closest approach to the site at the time of the upload. For the Lake Tahoe imagery all bands were acquired in daytime imaging, while only the mid- and thermal infrared bands, J, K, L, M, and N were acquired in nighttime imaging.

A few minutes prior to the acquisition, the MTI would predict its location at the time of the acquisition and begin reorienting to point at the site from this location. The pointing accuracy after this reorientation depended on the performance of the onboard laser gyros, whose performance degraded more rapidly than specified and were no longer usable by April 2001. While the gyros were operational, nadir pointing was within 2 km of the specifications, in both day and nighttime imagery, after the gyros were no longer usable, pointing was within 4 km in daytime imaging, and typically within 8 km in nighttime imaging.

The first Lake Tahoe images were approximate squares centered on the shore of the lake to allow georegistration. This was changed when it was recognized that no square image centered on the shoreline could consistently image all the buoys. The vast majority of the images therefore were about three times longer than they were wide with a center near that of the lake and included both the north and south shores of the lake. While the gyros were operational this format would include the locations of all four buoys in the northern half of the image. After the gyros failed, pointing errors, particularly in nighttime images, could cause one or two buoys to fall outside the eastern or western extent of the image. In addition, after the failure of the gyros, the detector arrays in nighttime images need not always be aligned perpendicular to the groundtrack, resulting in gaps between the SCA TIR subimages that could in turn result in one or two buoys missing data.

B. Standard MTI Image Data Processing

The acquired imagery was transmitted to the ground station at Sandia National Laboratories, and then processed at the data processing center, then located at Los Alamos National Laboratory. This imagery then underwent an initial processing that resulted in calibrated and registered imagery.

The aperture door largely eliminated on-orbit degradation of the MTI system prior to the loss of the TCAL unit. The sole exceptions were a few detector pixels that lost most of their response after thermal cycling of the focal plane. As a result calibrated imagery prior to the TCAL loss relied almost exclusively on the ground calibration data, and responses to the onboard calibration sources acquired concurrent with the imagery were largely used to verify system stability. An exception to this was the use of responses to the retromirror, in combination with responses to weekly deep space looks, to correct for drifts in the detector offsets.

After the loss of the TCAL unit, no onboard sources were available either for image calibration or for the validation of system stability. Deep-space looks were increased in frequency to once per orbit, and the most recent previous look was used directly to correct the TIR imagery for drifts in the detector offsets. The imagery subsequent to the TCAL loss showed artifacts in bands L, M, and N on SCAs 2 and 3 that were attributed to vignetting caused by the distortion of the optics after the loss of thermal control of the system. These artifacts are removed by using a form of vicarious calibration, termed the 90° look, to transfer the calibration of unvignetted detectors to the vignetted ones. Versions of the 90° looks were subsequently found to be useful in the correction of detector damage caused by the two Sun looks.

In the 90° looks for the TIR bands, the MTI is pointed at an ocean location well away from land. For convenience, these locations were selected from a set of ocean buoy locations that were being used for the validation of MTI water surface temperature retrievals. The detector arrays are rotated to be approximately parallel to the ground track, instead of perpendicular, and an image is acquired. In this image, the detectors in the arrays on SCAs 2 and 3 then pass over approximately the same band dependent location. The resulting imagery is then examined to eliminate images with detector drifts during the acquisition as these indicate spatial nonuniformity. Those images with negligible drifts are assumed to be imaging uniform temperature water surfaces, and the detector responses are assumed to be the same band dependent brightness temperatures, which are determined from the calibrated brightness temperatures for the unvignetted detector pixels. This analysis yields scale factors to correct the detector radiances estimated from the original ground calibration for simple vignetting.

TABLE IV
DATES OF IMAGES USED IN 90° LOOKS FOR VIGNETTING CORRECTION

Image	Date	Time UTC	Buoy Temperature (°C)
101621	1/28/2001	20:21:34	24.55
101659	1/31/2001	8:27:06	11.4
101805	2/8/2001	9:23:58	25
102348	2/28/2001	23:21:33	27.17
105565	7/31/2001	10:31:20	26.2
107615	11/12/2001	10:14:36	24.9
151778	6/9/2003	10:10:12	?

A number of usable 90° looks have been acquired. These are listed in Table IV, along with the acquisition date, time, and buoy temperature where available. The buoy associated with image 151 778 ceased reporting water temperatures in late May, when it was reporting temperatures near 25 °C. The calibration of a given image uses the most recent preceding 90 ° look, except for the earliest post-TCAL loss or post-Sun-look imagery, which use the first subsequent 90 ° look for their calibration.

The default registration of the MTI imagery is aligned with the image ground track, and relies on the information used by the satellite in pointing at the site, which had intrinsic errors of a few kilometers. Correction of this data for true georegistration requires manual analysis as discussed below. The registered data was resampled to form imagery with a 20-m ground sample distance using a weighted interpolation.

C. The Lake Tahoe Image Selection Process

The first MTI Lake Tahoe image was acquired on September 2, 2000. At the time of completion of this study 79 images had been acquired of Lake Tahoe, CA/NV. Thirty-six of these were daytime images and 43 were nighttime images. In terms of the major events that affected MTI calibration, two images were acquired before the TCAL loss, both daytime, 26 images between the TCAL loss and the first sun look (15 day and 11 night), 41 between sun looks (14 day and 27 night), and ten subsequent to the second sun look (five day and five night). Twenty-three cloud-free images were selected from the full set of acquisitions for validation. The other images were discarded due to cloud cover, poor pointing, or lack of field data.

The 23 images were then georegistered by applying an affine transform to the MTI imagery. The coefficients of this transform were determined manually by locating five or more corresponding points between the MTI image and a georeferenced image.

D. Lake Tahoe Buoy Specific Analysis

The selected georegistered images were subjected to a detailed buoy specific analysis. The buoy specific analysis had two parts: a manual quality analysis, and an automated data extraction process.

The data quality analysis focused on cloud cover issues, but also examined water surface temperature gradients that could cause errors in the interpretation of data due misidentification of the buoy location in the image. Because the buoy moorings were not taught, the buoy locations could differ from their nominal locations by more than 200 m. In cloud-free regions of daytime imagery, pixels brighter than the water surface were often observable in the high spatial resolution bands near the nominal buoy locations. These pixels were assumed to indicate the true buoy locations at the time of the image.

Cloud identification relied primarily on spatial structure in the thermal infrared imagery. Cloud-like colder structures that extended over a buoy's location were assumed to indicate cloud contamination for that buoy's data, and data from that buoy would be dropped from the analysis. This ensured that processing would be consistent between day and nighttime data. The band H (cirrus band) daytime data were also examined to confirm the results of the thermal image analysis. Confirmation failed for one daytime image acquired on April 14, 2001. While neither the band H nor the TIR imagery had significant spatial structure over the lake in this image, the band H radiances were more than a factor of three larger than radiances typical of cloud-free water surface images. Further the slightly darker areas in the band H imagery corresponded closely to the slightly warmer regions in the TIR imagery. It is currently believed that this image had either significant uniform low level haze, or extremely uniform cirrus.

The automated data extraction process took as its input data files containing the georegistered imagery and the buoy locations. It would identify the pixels in the imagery nearest the locations and extract 5×5 sample regions centered on these pixels, and then write a separate file for each buoy giving the band specific radiances for each of the pixels in this region, and statistical summaries including band specific means and standard deviations. The file also reported pixel specific data quality information such as the MTI sensor chip assembly (SCA) associated with the buoy image location. This study uses the nominal buoy locations for both day and nighttime imagery.

V. FIELD DATA PROCESSING

Initially the bulk water temperature was extracted from the temperature sensors placed ~ 2 cm beneath the surface on the float tethered behind each buoy at the time of the MTI overpasses. The bulk water temperature was calculated as the mean of the measured temperatures at the time of the overpass. Each buoy typically has four temperature sensors attached to the float but may have as many as 12 sensors. Prior to inclusion in the mean the temperature trace of each sensor was examined and cross-compared with the other sensors on the same buoy to check all sensors were reading correctly. The standard deviation of the sensors was also calculated and was typically around 0.1 °C (see Section VII).

In order to compare the radiometer measurements to the satellite radiometric measurements it is necessary to correct the field measurements to surface kinetic or skin temperature so they can be propagated through the atmosphere using the MODTRAN 3.5 radiative transfer code (RTC) [4]. Once propagated, the top of atmosphere radiance is convolved to the MTI system response functions and compared with the MTI radiances. The surface skin temperature is required since the field radiometers measure the radiometric temperature over a different wavelength range than the satellite radiometers. In order to obtain the surface skin temperature the radiometer data must be corrected for the reflected downwelling radiation from the atmosphere and the non unit emissivity of the water. Correction for the downwelling sky radiance reflected by the surface into the path of the radiometer involves using a radiative transfer model driven by an atmospheric profile to estimate the downwelling sky radiation and is described by Hook *et al.* [8], [9]. The atmospheric profile was obtained from the National Center for Environmental Prediction

TABLE V

CHANGE IN THE CALCULATED AT-SENSOR MTI RADIANCE AND AT-SENSOR MTI BRIGHTNESS TEMPERATURE FOR VARIOUS PERTURBATIONS OF THE U.S. STANDARD ATMOSPHERIC PROFILE AT THE LAKE TAHOE ELEVATION, WITH A SURFACE KINETIC TEMPERATURE OF 20.0 °C, AND THE MTI BAND J AND K SPECTRAL RESPONSE FUNCTIONS. NADIR VIEWING IS THE NOMINAL CASE FOR ALL DIFFERENCES EXCEPT POINTED WHERE 5° FROM NADIR IS USED FOR THE POINTING ANGLE SENSITIVITY. THE $-5°$ POINTING ANGLE CASE MOVES BACK TO NADIR, WHILE THE $+5°$ CASE MOVES FIVE MORE DEGREES AWAY FROM NADIR. THE WATER EMISSIVITY SPECTRUM USED IN THIS STUDY USES 0.991 FOR THE EMISSIVITY OF WATER BETWEEN 10.7 AND 11.2 μm. WHEN ADDING 0.01 TO THE EMISSIVITY, THE RESULTING VALUES WERE TRUNCATED TO 1.000 IN THIS RANGE

Change from Nominal in Radiance and Brightness Temperature	Adjusted radiance (J)	Radiance Difference (J)	% Radiance Difference (J)	Temperature Difference (°C) (J)	Adjusted radiance (K)	Radiance Difference (K)	% Radiance Difference (K)	Temperature Difference (°C) (K)
90% Water Vapor	0.363	0.0005	0.14	0.031	1.4803	0.0271	1.86	0.514
110% Water Vapor	0.362	-0.0005	-0.14	-0.031	1.4276	-0.0256	-1.76	-0.493
-1 deg C	0.3617	-0.0008	-0.22	-0.05	1.4439	-0.0093	-0.64	-0.178
+1 deg C	0.3633	0.0008	0.22	0.05	1.4629	0.0097	0.67	0.185
50% Ozone	0.3625	0	0	0	1.4543	0.0011	0.08	0.021
150% Ozone	0.3625	0	0	0	1.452	-0.0012	-0.08	-0.023
50% Visibility (11.5 km)	0.3588	-0.0037	-1.02	-0.231	1.444	-0.0092	-0.63	-0.176
150% Visibility (34.5 km)	0.3637	0.0012	0.33	0.074	1.4562	0.003	0.21	0.057
-5 deg pointing	0.3623	0.0002	0.06	0.012	1.4521	0.0011	0.08	0.021
+5 deg pointing	0.3619	-0.0004	-0.11	-0.025	1.4488	-0.0033	-0.22	-0.063
-0.01 emissivity	0.3591	-0.0034	-0.94	-0.212	1.4431	-0.0101	-0.7	-0.194
+0.01 emissivity	0.3659	0.0034	0.94	0.211	1.4633	0.0101	0.7	0.193

The nominal or original radiance for bands J and K was 0.3625 and 1.4532 respectively. All radiances in W/m2.sr.μm

(NCEP). The NCEP produces global model values on a $1° \times 1°$ grid at 6-h intervals. Lake Tahoe is centered on 39 N, 120 W, and the grid value for this point was utilized. The NCEP data were interpolated to the overpass time. The emissivity of the water was obtained from the ASTER spectral library available from http://speclib.jpl.nasa.gov.

In some cases, the skin temperature was not available at *any* buoy for a given overpass or for a particular buoy on a given overpass. If no skin (radiometer) temperatures were available for *any* buoys for a given overpass, the average skin effect (bulk minus skin temperature) for *all* overpasses was subtracted from the average bulk temperature at each buoy to obtain the buoy skin temperature. If skin temperatures were available at some buoys, but not all buoys for a given overpass, then the average skin effect (bulk minus skin temperatures) for *that* overpass was calculated and subtracted from the bulk temperatures to obtain the skin temperatures for the buoys without a working radiometer. The bulk and skin temperatures are available from the lead author on request.

The skin temperatures were then propagated to at-sensor radiance using the same RTC code and profile used to correct the radiometric data to skin temperature and the at-sensor radiance was convolved with the MTI system response functions to obtain an equivalent predicted or vicarious MTI at-sensor radiance.

The need to correct the radiometric temperature to skin temperature with a downwelling radiance derived from the NCEP data introduces an uncertainty in the skin temperature. This uncertainty is very small (< 0.05 °C) and is discussed more fully by Hook *et al.* [8].

VI. FORWARD PROPAGATION UNCERTAINTY ANALYSIS

In order to calculate the vicarious at-sensor radiance, the skin temperature is propagated through the atmosphere using a RTC. In the propagation to at-sensor radiance, the atmospheric path length is the distance from the skin to the satellite as opposed to the distance from the radiometer to the skin, used to correct the radiometer temperature to skin temperature, and therefore the uncertainty is larger. Further, the size of this uncertainty is dependent on the wavelength position and width of the band that the at-sensor radiance is convolved with, in this case the MTI bands. Tables V and VI and Fig. 2 show the results from an assessment of the uncertainty associated with propagating the skin temperature to the satellite using a U.S. Standard Atmosphere for the MTI mid- and thermal infrared bands, respectively. A U.S. Standard Atmosphere contains more water vapor than is typically encountered at Lake Tahoe, and therefore the reported uncertainties represent the maximum uncertainty. The assessment involves modifying the various profile inputs and then calculating the difference between using the actual profile and the modified profile. This approach assesses the consequences of an error in the profile used to forward model the skin temperature to at-sensor radiance. For example, if the temperature profile is assumed to be in error by 1 °C, then 1 °C can be added to the profile, and the difference between the forward propagated radiance using the nominal and adjusted profiles calculated, similarly 1 °C can be subtracted from the profile and the difference between the forward propagated radiance using the nominal and adjusted profile calculated. It can be seen from Tables V and VI and Fig. 2 that different bands are more or less sensitive to a given profile error than other bands. For example, band K is more sensitive than the other bands to an error in either water vapor or profile temperature. Further, an error in the amount of ozone in the profile has little effect on any of the bands except band M since its bandpass impinges on the ozone absorption band. The thermal infrared bands are more sensitive than the mid-infrared bands to an error in emissivity, especially band N. However, since these data were acquired over water the emissivity of water is well known. The emissivity of water does vary with large viewing angles and varying wind speeds but with near-nadir viewing its emissivity is constant and well known [25].

TABLE VI

CHANGE IN THE CALCULATED AT-SENSOR MTI RADIANCE AND AT-SENSOR MTI BRIGHTNESS TEMPERATURE FOR VARIOUS PERTURBATIONS OF THE U.S. STANDARD ATMOSPHERIC PROFILE AT THE LAKE TAHOE ELEVATION, WITH A SURFACE KINETIC TEMPERATURE OF 20.0 °C, AND THE MTI BAND L, M, AND N A CASE FOR ALL DIFFERENCES EXCEPT POINTED WHERE 5° FROM NADIR IS USED FOR THE POINTING ANGLE SENSITIVITY. THE −5° POINTING ANGLE CASE MOVES BACK TO NADIR, WHILE THE +5° CASE MOVES FIVE MORE DEGREES AWAY FROM NADIR. THE WATER EMISSIVITY SPECTRUM USED IN THIS STUDY USES 0.991 FOR THE EMISSIVITY OF WATER BETWEEN 10.7 AND 11.2 μm. WHEN ADDING 0.01 TO THE EMISSIVITY, THE RESULTING VALUES WERE TRUNCATED TO 1.000 IN THIS RANGE

Change from Nominal in Radiance and Brightness Temperature	Adjusted radiance (L)	% Radiance Difference (L)	Temperature Difference (°C) (L)	Adjusted radiance (M)	% Radiance Difference (M)	Temperature Difference (°C) (M)	Adjusted radiance (N)	% Radiance Difference (N)	Temperature Difference (°C) (N)
90% Water Vapor	7.18	0.46	0.217	7.752	0.27	0.136	8.515	0.13	0.079
110% Water Vapor	7.115	-0.45	-0.211	7.709	-0.28	-0.142	8.491	-0.15	-0.094
-1 deg C	7.134	-0.18	-0.086	7.72	-0.14	-0.071	8.5	-0.05	-0.029
+1 deg C	7.16	0.18	0.086	7.742	0.14	0.071	8.508	0.05	0.029
50% Ozone	7.15	0.04	0.02	7.784	0.69	0.342	8.509	0.06	0.036
150% Ozone	7.144	-0.04	-0.02	7.681	-0.65	-0.324	8.498	-0.07	-0.043
50% Visibility	7.124	-0.32	-0.152	7.681	-0.65	-0.324	8.465	-0.46	-0.281
150% Visibility	7.155	0.11	0.053	7.748	0.22	0.11	8.516	0.14	0.086
-5 deg pointing	7.145	0.03	0.013	7.729	0.03	0.013	8.503	0.01	0.007
+5 deg pointing	7.138	-0.1	-0.046	7.723	-0.08	-0.039	8.5	-0.04	-0.022
-0.01 emissivity	7.09	-0.8	-0.376	7.664	-0.87	-0.434	8.425	-0.93	-0.57
+0.01 emissivity	7.204	0.8	0.374	7.797	0.85	0.425	8.577	0.86	0.524
The nominal or original radiance for bands L, M and N was7.147, 7.731 and 8.504 respectively. All radiances in W/m2.sr.μm									

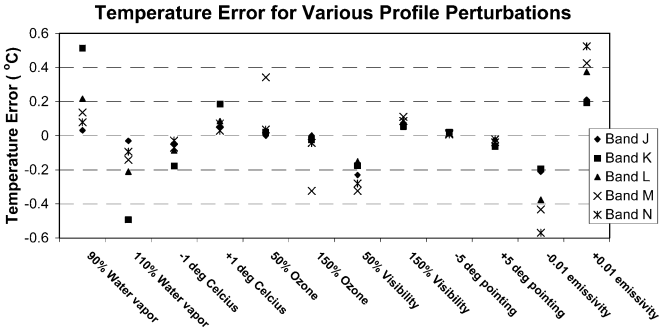

Fig. 2. Plot of the temperature error associated with perturbing the atmospheric profile, varying the path length (pointing error), and assuming an incorrect emissivity for the MTI bands. The errors for the profile perturbations were obtained by calculating the at-sensor radiance for a U.S. standard atmospheric profile over Lake Tahoe, then modifying the profile and recalculating the at-sensor radiance and calculating the brightness temperature difference between the at-sensor radiances.

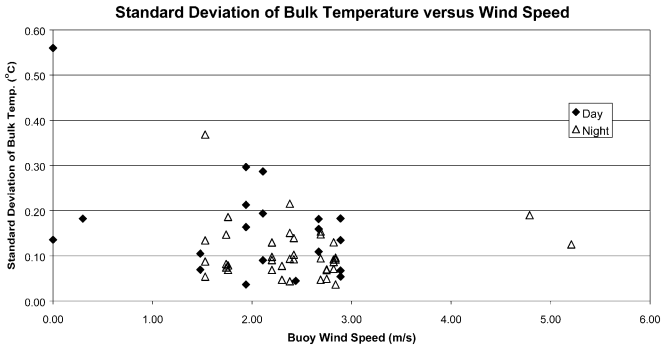

Fig. 3. Plot of the standard deviation of the bulk temperature sensors at each of the Lake Tahoe buoys versus wind speed for the MTI overpass times. Data are separated into day and night standard deviations. Wind speed data used was either from the USCG station or the buoy meteorological station. The buoy data were used if no USCG data were available.

Based on a qualitative assessment of model profile values with in situ measurements (balloon launches) there can be considerable variability in the water profile values but the balloon-derived temperature profile values are typically in good agreement with the modeled values. Therefore, sites with little water vapor in the overlying atmosphere, such as Lake Tahoe site, are desirable for validation since this quantity can vary between the model and *in situ* values. The total column water vapor on clear days at Lake Tahoe is typically between 0.5–1.5 cm.

VII. RESULTS AND DISCUSSION

The measurements made at the buoys include both skin temperature and bulk temperature measured by the radiometers and the *in situ* temperature probes, respectively. The skin temperature measurement is propagated through the atmosphere to obtain the equivalent radiance at-sensor used for the forward calculation rather than the bulk temperature since the satellite measures the skin temperature. Fig. 3 shows a plot of the standard deviation of the bulk temperature sensors versus the wind speed measured at the buoys for the MTI overpasses. The wind speeds

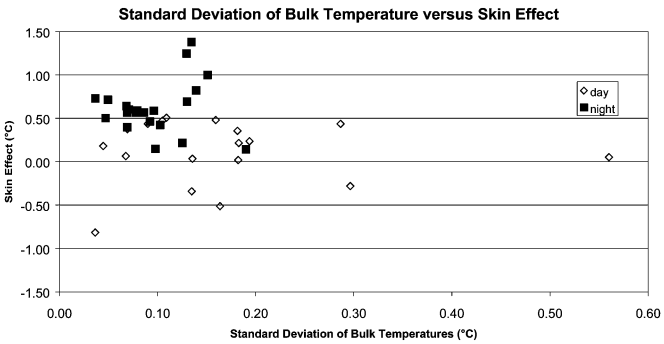

Fig. 4. Plot of the skin effect (bulk temperature minus skin temperature) versus standard deviation of the bulk temperature sensors at each of the Lake Tahoe buoys for the MTI overpass times.

for the majority of validations were between 1.5 and 3.0 $\mathrm{m \cdot s^{-1}}$ with standard deviations between 0.03 and 0.3. Fig. 4 shows a plot of the skin effect versus standard deviation. The skin effect is the difference between the bulk temperature and the skin temperature. The daytime skin effect is typically smaller than the nighttime skin effect, and the standard deviation is often larger

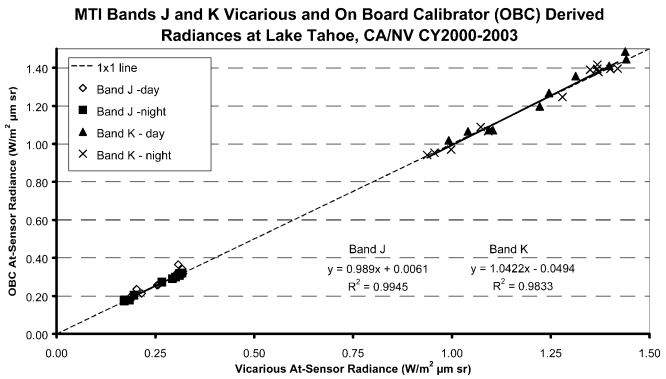

Fig. 5. Plot of MTI OBC-derived average at-sensor radiances versus vicarious (predicted) average at-sensor radiances for MTI bands J and K centered on 3.79 and 4.98 μm, respectively. Averages are calculated using data from all operational buoys for a given overpass (maximum of four buoys). Data are separated into day predictions and night predictions. Also shown is a linear fit to the night data only for bands J and K. Dashed line is the 1×1 line (shown for reference).

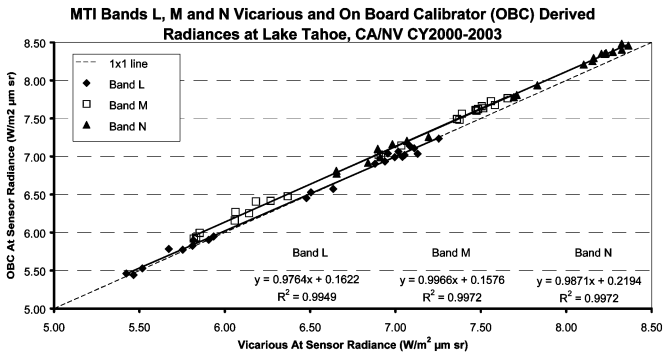

Fig. 6. Plot of MTI OBC-derived average at-sensor radiances versus vicarious (predicted) average at-sensor radiances for MTI bands L, M, and N centered on 8.28, 8.65, and 10.52 μm, respectively. Averages are calculated using data from all operational buoys for a given overpass (maximum of four buoys). Also shown are linear fits to the data from each band. Dashed line is the 1×1 line (shown for reference).

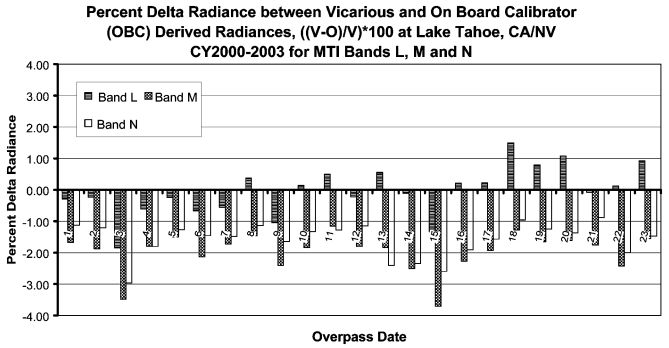

Fig. 7. Plot of the average percent difference between the Vicarious (V) and MTI OBC-derived radiances for MTI bands L, M, and N. Percent difference is calculated as (V-OBC)/V $*$ 100. Average percent difference is calculated from all buoys operating during overpass (maximum of four buoys).

during the day. The smaller skin effect and larger standard deviation during the day typically results from solar heating of the surface accompanied by low wind speeds, resulting in rapid stratification of the surface layer. The size of this effect varies with time of day and local meteorological conditions. The skin effect is discussed in more detail in [8] and [9]. The skin temperature was found to be 0.18 ± 0.36 °C cooler than the bulk temperature during the day and 0.65 ± 0.31 °C cooler than the bulk temperature at night for the MTI overpass time. It should be noted this is the average skin effect for an average time since the satellite overpass time has varied by a couple of hours over the lifetime of the mission. The daytime skin effect is similar to that observed for Landsat $(0.26 \pm 0.49$ °C) and ASTER $(0.14 \pm 0.52$ °C) and is consistent with the MTI overpass time being closer to the ASTER overpass time than the Landsat overpass time although there is greater variability in the MTI overpass time. The nighttime overpass time is similar to that of ASTER, and the MTI skin effect is similar to the ASTER nighttime skin effect $(0.4 \pm 0.24$ °C). These values falls within the nominal range for the skin effect observed over oceans [6], [7], [11], [12], [16], [19], [20], [24].

Fig. 5 shows a plot of the predicted or vicarious at-sensor radiances and measured or MTI On-Board Calibrator (OBC) radiances for the mid-infrared bands for the MTI overpass times. A single value is shown for each overpass that is the average of the vicarious or measured at-sensor radiances for a given band for all buoys (maximum of four buoys in a scene). Twenty-three cloud-free MTI scenes were acquired over Lake Tahoe, but, for the mid-infrared analysis only the nighttime data were used to avoid any reflected solar contribution to the signal which is not accounted for in the forward prediction. No attempt was made to account for any possible contribution from moon light. Also shown on Fig. 5 are least squares fit lines to the band J and K nighttime data and the associated fit coefficients. Examination of Fig. 5 indicates there is greater scatter in the band K data than the band J data possibly due to the greater sensitivity to any errors in the atmospheric profile data in this wavelength region and stronger solar effects. Neither the band J nor band K daytime data are visually noticeably different than the nighttime data, however, a fit to all the band K data which includes data affected by solar reflected radiation, does increase the difference between the OBC and vicarious at-sensor values. The mean and standard deviation of the percent difference between the vicarious and OBC radiances for bands J and K were -1.38 ± 2.32 and -2.46 ± 1.96, respectively.

Fig. 6 shows the equivalent plot for to Fig. 5 for the MTI thermal bands using all 23 cloud-free scenes (daytime and nighttime). The results indicate the OBC radiances in band L are in excellent agreement with the vicarious radiances, however, the OBC radiances for bands M and N are biased positive with respect to the equivalent vicarious radiances indicating the MTI overestimates the radiance arriving at the sensor from the surface in bands M and N. This bias is even more apparent in a plot of the percent radiance difference with overpass date (Fig. 7). In Fig. 7 the bias is reasonably consistent except for a couple of outliers labeled 3 and 15. The data for label 3 were acquired on March 27, 2001, at that time none of the radiometers were functioning and an average skin effect was used. The larger than expected bias likely results from the assumed skin effect being an overestimate of the actual skin effect. The data for label 15 were acquired on April 3, 2002, at that time only a single radiometer on TB1 was operating and therefore the skin effect used for the other buoys was assumed to be the same as the skin effect observed at TB1. The skin effect at TB1 was unusually large; the radiometer data were 1.38 °C cooler than the bulk temperature. The wind speed measured at TB1 at the same time the radiometer measurement was made was 0.0 (the stall speed of the anemometer is 0.25 m $\cdot$ s^{-1}, according to manufacturer's

specifications). At very low wind speeds the skin effect is quite variable and it is likely the skin effect was less at the other buoys which had higher wind speeds than TB1. The results indicate the mean and standard deviation of the percent difference between the predicted and measured radiances were -0.04 ± 0.78, -1.97 ± 0.62, -1.59 ± 0.55 for bands L through N, respectively.

The cause of the biases observed in MTI bands J, K, M, and N is unresolved, but the biases appear to be consistent over the instrument's lifetime, suggesting they could be removed with a bias correction. The radiometric calibration of the instrument does not appear to have changed during the accidental viewings of the Sun.

VIII. Summary and Conclusion

The absolute radiometric calibration of the MTI mid- and thermal infrared bands was assessed from late 2000 through 2003 using water skin and bulk temperature data from an automated validation site at Lake Tahoe CA/NV, USA. The bulk and skin temperature data are acquired every 2 min from four permanently moored buoys on the lake. Assessment involved taking the skin temperature at the time of the overpass and predicting the vicarious at-sensor radiance with a radiative transfer model. The vicarious at-sensor radiance was then convolved with the MTI system response function and compared with the radiance measured by MTI in the mid- and thermal infrared bands. Twenty-three cloud-free scenes were used in the assessment with ground temperatures ranging between 4.4 and 18.6 °C. All 23 scenes were used in the assessment of the thermal infrared bands and only the twelve nighttime scenes were used in the assessment of the mid-infrared data to avoid any reflected solar contribution which was not included in the forward predictions.

The skin temperature was found to be, on average, 0.18 ± 0.36 °C (mean ±1 standard deviation) cooler than the bulk temperature during the day and 0.65 ± 0.31 °C cooler than the bulk temperature at night. The smaller skin effect during the day was attributed to solar heating. The daytime skin effect is similar to that observed for the Landsat-5 and ASTER daytime overpass times: 0.26 ± 0.49 and 0.14 ± 0.52 °C, respectively. The smaller skin effect is consistent with the MTI overpass time being closer to the ASTER overpass time when the skin has warmed through solar heating. The nighttime overpass time is similar to that of ASTER (0.4 ± 0.24 °C).

The results indicate the mean and standard deviation of the percent difference between the vicarious (predicted) and measured MTI at-sensor radiances were -1.38 ± 2.32, -2.46 ± 1.96, -0.04 ± 0.78, -1.97 ± 0.62, -1.59 ± 0.55 for bands J through N, respectively. The exact reason why the MTI measured radiances for bands J, K, M, and N are warmer than expected has not been identified, however, since the biases seem quite consistent it should be possible to apply a simple offset correction to the data.

MTI data provide the highest spatial resolution mid- and thermal infrared data currently available from space and offer an opportunity to examine the use of high spatial resolution temperature data for a wide variety of studies. However, if the data are to be used in quantitative studies it will be necessary to adjust the radiances to compensate for the biases observed by the in-flight validation. Further, continued monitoring of the in-flight validation is required to ensure the observed biases remain consistent as the instrument ages.

Acknowledgment

Numerous people have contributed to this work. In particular, the authors would like to thank the UCD Tahoe Research Group and F. Palluconi for providing numerous helpful suggestions.

References

[1] J. A. Barsi, J. R. Schott, F. D. Palluconi, D. L. Helder, S. J. Hook, B. L. Markham, G. Chander, and E. M. O'Donnell, "Landsat TM and ETM+ thermal band calibration," *Can. J. Remote Sens.*, vol. 29, pp. 141–153, 2003.

[2] I. J. Barton, P. J. Minnett, K. A. Maillet, C. J. Donlon, S. J. Hook, A. T. Jessup, and T. J. Nightingale, "The Miami2001 infrared radiometer calibration and inter-comparison: Ship comparisons," *J. Atmos. Oceanic Technol.*, vol. 21, pp. 268–283, 2004.

[3] I. J. Barton, "Satellite-derived sea-surface temperatures—Current status," *J. Geophys. Res.—Oceans*, vol. 100, pp. 8777–8790, 1995.

[4] A. Berk, L. S. Bernstein, and D. C. Robertson, "MODTRAN: A moderate resolution model for LOWTRAN 7," Geophys. Lab., Bedford, Mass., Tech. Rep. GL-TR-89-0122, 1989.

[5] W. B. Clodius, S. C. Bender, W. H. Atkins, W. Christensen, C. K. Little, R. R. Kay, and D. Bridenstine, "Initial MTI on-orbit calibration performance," *Proc. SPIE*, vol. 4132, pp. 290–305, 2000.

[6] C. J. Donlon and I. S. Robinson, "Radiometric validation of ERS-1 along track scanning radiometer average sea surface temperature in the Atlantic Ocean," *J. Atmos. Oceanic Technol.*, vol. 15, pp. 647–660, 1998.

[7] C. W. Fairall, E. F. Bradley, J. S. Godfrey, G. A. Wick, J. B. Edson, and G. S. Young, "Cool-skin and warm-layer effects on sea surface temperature," *J. Geophys. Res.—Oceans*, vol. 101, pp. 1295–1308, 1996.

[8] S. J. Hook, A. J. Prata, R. E. Alley, A. Abtahi, R. C. Richards, S. G. Schladow, and S. Ó. Pálmarsson, "Retrieval of lake bulk and skin temperatures using Along-Track Scanning Radiometer (ATSR-2) data: A case study using Lake Tahoe, California," *J. Atmos. Oceanic Technol.*, vol. 20, pp. 534–548, 2003.

[9] S. J. Hook, G. Chander, J. A. Barsi, R. E. Alley, A. Abtahi, F. D. Palluconi, B. L. Markham, R. C. Richards, S. G. Schladow, and D. L. Helder, "In-flight validation and recovery of water surface temperature with Landsat 5 thermal infrared data using an automated high altitude lake validation site at Lake Tahoe CA/NV, USA," *IEEE Trans. Geosci. Remote Sens.*, vol. 42, no. 12, pp. 2767–2776, Dec. 2004.

[10] R. R. Kay, T. D. Henson, J. L. Rienstra, M. L. Decker, N. G. Rackley, P. J. Claassen, R. E. Kidner, R. B. Taplin, D. M. Bullington, K. D. Marbach, C. E. Lanes, B. C. Brock, P. G. Weber, S. C. Bender, B. W. Smith, W. B. Clodius, and C. C. Borel, "Multispectral Thermal Imager (MTI) payload overview," *Proc. SPIE*, vol. 3753, pp. 347–358, 2000.

[11] K. B. Katsaros, "Sea-surface temperature deviation at very low wind speeds—Is there a limit," *Tellus*, vol. 29, pp. 229–239, 1997.

[12] K. B. Katsaros, W. T. Liu, J. A. Businger, and J. E. Tillman, "Heat-transport and thermal structure in interfacial boundary-layer measured in an open tank of water in turbulent free convection," *J. Fluid Mech.*, vol. 83, pp. 311–311, 1977.

[13] C. H. Mortimer, "Water movements in lakes during summer stratification; Evidence from the distribution of temperature in windermere," *Phil. Trans. R. Soc. London*, vol. B236, pp. 355–404, 1952.

[14] S. G. Monismith, "Wind-forces motion in stratified lakes and their effect on mixed-layer shear," *Limnol. Oceanogr.*, vol. 30, pp. 771–783, 1985.

[15] ——, "An experimental study of the upwelling response of stratified reservoirs to surface shear stress," *J. Fluid Mech.*, vol. 171, pp. 407–439, 1986.

[16] M. J. Murray, M. R. Allen, C. J. Merchant, A. R. Harris, and C. J. Donlon, "Direct observation of the skin-bulk SST variability," *Geophys. Res. Lett.*, vol. 27, pp. 1171–1174, 2000.

[17] J. P. Rice, J. J. Butler, B. C. Johnson, P. J. Minnett, K. A. Maillet, T. J. Nightingale, S. J. Hook, A. Abtahi, C. J. Donlon, and I. J. Barton, "The Miami2001 infrared radiometer calibration and intercomparison," *J. Atmos. Oceanic Technol.*, pt. I: Laboratory characterization of blackbody targets, vol. 21, pp. 258–267, 2004.

[18] V. V. Salomonson, W. L. Barnes, P. W. Maymon, H. E. Montgomery, and H. Ostrow, "MODIS: Advanced facility instrument for studies of the Earth as a system," *IEEE Trans. Geosci. Remote Sens.*, vol. 27, no. 2, pp. 145–153, Mar. 1989.

[19] P. Schluessel, H. Y. Shin, W. J. Emery, and H. Grassl, "Comparison of satellite-derived sea-surface temperatures with in situ skin measurements," *J. Geophys. Res.—Oceans*, vol. 92, pp. 2859–2874, 1987.
[20] A. V. Soloviev and P. Schlussel, "Evolution of cool skin and direct air–sea gas transfer coefficient during daytime," in *Bound.-Layer Meteorol.*, 1996, vol. 77, pp. 45–68.
[21] P. T. Strub and T. M. Powell, "Wind-driven surface transport in stratified closed basins: Direct versus residual calculation," *J. Geophys. Res.*, vol. 91, pp. 8497–8508, 1986.
[22] ——, "Surface temperature and transport in Lake Tahoe: Inferences from satellite (AVHRR) imagery," *Continent. Shelf Res.*, vol. 7, pp. 1001–1013, 1987.
[23] Y. Yamaguchi, A. B. Kahle, H. Tsu, T. Kawakami, and M. Pniel, "Overview of Advanced Spaceborne Thermal Emission Reflectance Radiometer," *IEEE Trans. Geosci. Remote Sens.*, vol. 36, no. 4, pp. 1062–1071, Jul. 1998.
[24] G. A. Wick, W. J. Emery, L. H. Kantha, and P. Schlussel, "The behavior of the bulk-skin sea surface temperature difference under varying wind speed and heat flux," *J. Phys. Oceanogr.*, vol. 26, pp. 1969–1988, 1996.
[25] X. Q. Wu and W. L. Smith, "Emissivity of rough sea surface for 8–13 μm: Modeling and verification," *Appl. Opt.*, vol. 36, pp. 2609–2619, 1997.
[26] A. M. Zavody, C. T. Mutlow, and D. T. Llewellyn-Jones, "A radiative transfer model for SST retrieval for the ATSR," *J. Geophys. Res.*, vol. 100, pp. 937–952, 1995.

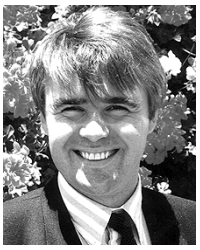

Simon J. Hook received the B.Sc. degree from the University of Durham, Durham, U.K., the M.Sc. degree from the University of Alberta, Edmonton, AB, Canada, and the Ph.D. degree from the University of Durham, in 1982, 1985, and 1989, respectively, all in geology.

From 1989 to 1991, he was a National Research Council Resident Research Associate wih the National Aeronautics and Space Administration Jet Propulsion Laboratory (JPL), Pasadena, CA. Since 1991, he has been a Technical Staff Member at JPL. From 1993 to 2003, he was the Project Scientist for the Advanced Spaceborne Thermal Emission and Reflectance Radiometer (ASTER). In addition to his work on ASTER, he has been involved in the validation of several airborne and spaceborne instruments, including Landsat-5 and ETM+, the Moderate Resolution Imaging Spectroradiometer (MODIS), MASTER (the MODIS/ASTER Airborne Simulator), the European Along-Track Scanning Radiometers (ATSR2 and AATSR), and the DOE Multispectral Thermal Imager. His research is focused on the use of solar reflective and thermal infrared remotely sensed data in geology and ecology with a special emphasis on in-flight calibration and validation.

William B. Clodius received the B.Sc. M.Sc., and Ph.D. degrees from the University of Delaware, Newark, in 1975, 1979, and 1982, respectively, all in physics.

From 1982 to 1983, he was a Postdoctoral Fellow at Texas Tech University, Lubbock. From 1983 to 1984, he was a Postdoctoral Fellow at the University of Utah, Salt Lake City. Since August 1984, he has been a Technical Staff Member with the Los Alamos National Laboratory, Los Alamos, NM. He has been involved in remote sensing since 1992, when work began on the Multispectral Thermal Imager (MTI). In addition to his work on the MTI, he has worked on ion photodetachment, the spectroscopy of symmetric molecules, the analysis of the optical and radio-frequency (RF) signatures of nuclear weapons and particle beams, the analysis of backgrounds for RF systems, hyperspectral system modeling, and hyperspectral system design.

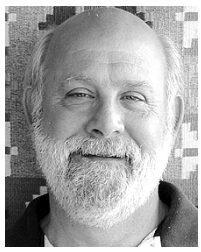

Lee K. Balick received the B.S. degree in physical science, the M.S. degree in atmospheric science, and the Ph.D. degree in forest science from Colorado State University, Fort Collins, in 1969, 1971, and 1978, respectively.

He is currently an Interdisciplinary Researcher in remote sensing science and applications. Since receiving his Ph.D., he has been working on remote sensing R&D for environmental, defense, and intelligence applications. During this time, he has worked for the U.S. Army Corps of Engineers, the U.S. Geological Survey EROS Data Center, the U.S. Department of Energy's Remote Sensing Laboratory, and the Los Alamos National Laboratory. The emphasis of his work has been on the phenomenology of thermal and reflected signatures including modeling, measurement, and image processing. He has extensive experience with airborne and satellite multispectral and thermal imaging sensors and the exploitation of these data for a variety of applications. He has served as the LANL Science Team Leader for the Multispectral Thermal Imager during its in-service R&D phase and worked closely with the U.S. ASTER Science Team. His current research interests include broad-area scene simulation, the inclusion of signature phenomenology in detection methodology, hyperspectral thermal IR hyperspectral phenomenology of the earth surface, landmine and camouflage detection, and environmental impacts on remote sensing for security and nonproliferation applications.

Ronald E. Alley, photograph and biography not available at the time of publication.

Ali Abtahi, photograph and biography not available at the time of publication.

Robert C. Richards received the B.A. and M.A. degrees in zoology from the University of California, Davis (UC Davis) in 1961 and 1989, respectively.

He is currently a Research Limnologist with UC Davis. He has been a coauthor or lead author on over 27 research papers and has given oral presentations at international, national, and regional limnological meetings.

S. Geoffrey Schladow is a Professor of civil and environmental engineering at the University of California (UC Davis), Davis, and Director of the UC Davis Tahoe Environmental Research Center. His research interests include mixing and transport processes in aquatic systems, water quality modeling, and the linkages between fluid mechanics and the determinants of water quality and ecological well-being.